Energy-Filtering Transmission Electron Microscopy of Biological Specimens

W. C. de Bruijn
Erasmus University Rotterdam

C. W. J. Sorber
Erasmus University Rotterdam

E. S. Gelsema
Erasmus University Rotterdam

A. L. D. Beckers
Erasmus University Rotterdam

J. F. Jongkind
Erasmus University Rotterdam

Utah State University
MERRILL-CAZIER LIBRARY

ENERGY-FILTERING TRANSMISSION ELECTRON MICROSCOPY OF BIOLOGICAL SPECIMENS

W.C. de Bruijn[*], C.W.J. Sorber, E.S. Gelsema[1], A.L.D. Beckers[1], J.F. Jongkind[2]

A.E.M. unit, Pathological Institute, [1]Dept. of Medical Informatics, and [2]Dept. of Cell Biology and Genetics,
Erasmus University Rotterdam, Medical Faculty and Health Sciences,
P.O. Box 1738, 3000 DR Rotterdam, The Netherlands

Abstract

By energy-filtering transmission electron microscopy (EFTEM) electrons can be separated by their energy losses. An electron-energy filter, added to the microscope column allows the measurement of the energy distribution of transmitted electrons that have lost energy ($< 2,000$ eV, with an energy resolution of ~ 1 eV). These filtered electrons, recorded either as a spectrum or as an image, are composed of two parts superimposed on top of each other: (a) the unspecific energy-loss population (= the continuum) and (b) the specific element-related energy-loss population (= the edges). At the edges, electron data in spectra and images are mathematically processed, to obtain the desired element-related net-intensity values or images. These data are related to the total transmitted electron intensity, from the zero- and low-loss spectral region giving the relative spectral- or image intensity ratios ($^SR^*_x$, $^IR^*_x$), which can be related to the element concentration. The acquisition of the zero-loss and low-loss data is hampered by the restricted dynamic range of the TV camera. By improvements through the introduction of calibrated attenuation filters in the optical path to the TV-camera, more reliable values for $^SR^*_x$ and $^IR^*_x$ can be acquired. By addition of Bio-standards adjacent to the tissue, a "known" and "unknown" concentration of the element present in the same ultrathin section and the "bias" in the concentration estimation, can be obtained. Some practical examples are given for the estimation of the iron concentration in siderosomes, boron in melanosomes and calcium in calcium oxalate monohydrate crystals.

Key Words: Energy-filtered transmission electron microscopy, Bio-standards, biological materials, light-attenuation filters, ferritin particles, calcium oxalate monohydrate crystals.

[*]Address for correspondence:
W.C. de Bruijn,
AEM-unit, Pathological Institute, Ee 902,
Erasmus University Rotterdam, P.O.Box 1738,
3000 DR Rotterdam, The Netherlands.
 Telephone no.: (31) 010-4087922; Fax: 010-4366660

Introduction

In electron microscopes, incident electrons from the electron gun may interact with the atoms of the (biological) material in a variety of ways. Single and multiple, elastic and inelastic scattering events may take place. A result of these events is that the incident electrons lose energy. The degree of energy-loss with respect to the travelled distance (section thickness, t) has been related to parameters of the material [35, 40]. When the layer of material is extremely thin, incident electrons may pass the material without any or just one single interaction. In that case, the number of transmitted zero-loss electrons relative to the number of incident electrons, is dependent on the material's thickness. By ignoring the elastically-scattered electrons, the energy losses of inelastically scattered electrons disclose the nature of the elements or chemical bonds present in the irradiated area. In the total population of the transmitted inelastic electrons, the majority of the energy-losses cannot be related to a definable element or a chemical bond. These electrons form a continuum, steadily deceasing in energy. The inelastic electron population, which can be related to element-specific interactions, once recorded, is observed as irregularities, called edges, at defined positions in this continuum pattern [35]. It is beyond the scope of this review to describe the details of the physics behind these events. This review will be restricted to the aspects of the spectrum- and image acquisition of the transmitted electrons. Hence, the instruments for recording will be limited to scanning and conventional transmission electron microscopes (STEM and CTEM). Electron optical aspects (covered in textbooks, e.g., see [35]) will also not be addressed.

Microscopes with energy-filtering capacities have in common that an electron spectrometer is incorporated, either in- or outside the column. Energy-filtered electron information can be recorded as spectra and/or images under both CTEM- and STEM conditions. In Figure 1, a CTEM cross-section is shown with an in-column spectrometer of the prism/mirror/prism type according to Castaing/Henry, in the modification of Ottensmeyer [35, 65]. Other magnetic-sector (Ω type) spectrometers
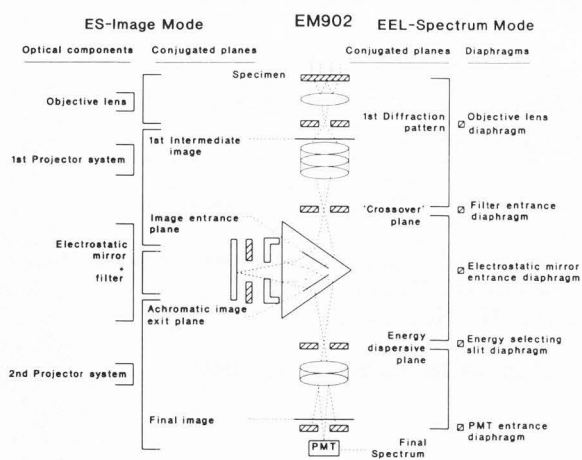
ES-Image Mode   EM902   EEL-Spectrum Mode

Figure 1. CTEM cross-section with an in-column spectrometer of the prism/mirror/prism-type according to Castaing/Henry/Ottensmeyer. Conjugate planes and the position of the various diaphragms are indicated at the left and right side.

[49, 67] are presently incorporated in one of the planes, conjugate with the back-focal plane of the objective lens. Out-column magnetic-sector spectrometers are generally placed in the conjugate plane below the final screen. Additional quadrupole and octupole lens systems may be added to obtain an image [48-50, 52]. From both instrument types, spectra are acquired as electron-intensity recordings related to energy-loss over, e.g., 0-2,000 eV. Spectra (electron energy-loss spectroscopy, EELS) can be recorded serially, with the use of counting devices, e.g., a photomultiplier tube (PMT), or in parallel, with a linear diode array or with a television (TV)- or charge-collection device (CCD) camera [36, 43].

When inhomogeneous specimens are analyzed, it is a prerequisite that the area from which the spectral information is derived can be indicated within a corresponding image. For the recording of element-related images, STEM instruments make use of the digital-beam scan mode. Multiple spectra are acquired from an array of analyzed areas (16^2 to 2048^2 spots) projected over a part of the specimen. The spectral information is stored digitally, on disk. From the stored spectra, an energy-filtered image can (off-line) be reconstructed or (on-line) projected on a screen or camera with the use of additional lens systems [11-15, 49, 50]. For image recording in the CTEM-instruments, multiple energy-loss related images have to be acquired, by projection on an image sensor (e.g., in a TV- or CCD camera). The intensity values, present in the images, have to be digitized (512^2 or 1024^2), to allow image operation and mutual comparison (off-line) [80]. The pros and cons of the two instrumental approaches are discussed in the literature [58, 59]. At the present state of the art, for *in situ* analysis of biological specimens, a CTEM/image combination may be preferred, because in such specimens a high de-

gree of local variation in items of interest is present and high magnifications with atomic resolution are mostly not required. The contrast-sensitive digital CTEM image resembles the conventional analogue micrograph and might be considered to represent a summation of several element-related image fractions. Qualitatively, it suffices to relate the localization of a single element in one image to the contrast-sensitive image, or to combine the localization of two or more element-related images. For that purpose, false-color images are made from the binary element-related images which are subsequently superimposed [1, 3, 4, 41, 42, 79].

The chemical elements to be detected in the cells and tissues, have to be preserved or protected against the influences of all steps in the tissue-preparation procedure, required for TEM. For the majority of biological materials, structural preservation by aldehyde-fixation is considered to be adequate. However, under such conditions only those endogenous elements can be investigated that have resisted both an aqueous dissolution during fixation and an organic-solvent dissolution during dehydration and embedding [53]. In (immuno)-cytochemistry and *in situ* hybridization, generally after aldehyde fixation, elements can be introduced into the tissue [17, 51, 78-80]. Such (reaction) products have to be protected against the dissolution phases that follow, to allow TEM observation.

Cryo-fixation, combined with freeze-drying or freeze-substitution plus conventional or low-temperature resin embedding is considered to preserve most, if not all, endogenous elements. Conventional wet-sectioning procedures have to be abandoned and replaced by dry-sectioning procedures [7, 31-34, 96, 98, 102-107]. The section thickness has to meet the requirements related to the mean free-path condition of energy-filtered transmission electron microscopy (EFTEM): one single scattering event per passage through the section. Attention has to be paid to the aspects of elemental dislocation, spatial resolution, and detection limits [29, 33, 106, 107].

This review concentrates upon the acquisition of quantitative morphometrical and/or chemical information from items of interest in cells by EFTEM. Qualitative and quantitative results acquired by a point-analysis/spectrum mode will be compared with those in the image-mode from the same type of material. The general question to be answered is: do both information streams give comparable results (which theoretically has to be the case). The aim is to show that for biological materials, irrespective of the answer to that question, much is to be gained from image analysis provided technical problems can be overcome and the reliability of the analyses by the image mode can be demonstrated. In this paper, various aspects (slit-width; slit-positions around the edge; addition, subtraction or division of images; width of the integration zone; number of images in the fitting zone) related to a comparison between results acquired by spectra and by images are investigated. The proposed quantitation procedure will be restricted to cells

Figure 2. Schematic cross-section of the lower part of the CTEM 902 microscope in which the components of the image analysis chains are shown in relation to the Olivetti personal computer (M280) and the IBAS.
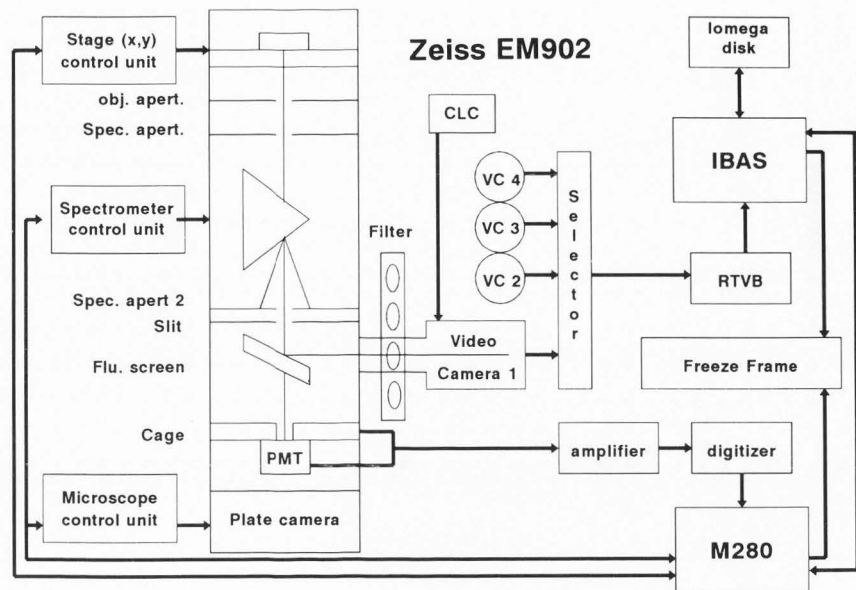
and tissues in which the endogenous elements have resisted aldehyde fixation, resin-embedding and wet-sectioning procedures. With Bio-standards added to the tissue prior to embedding, and present in the same ultrathin section, the "bias" in the concentration determination has also been determined.

Materials and Methods

In our laboratory, EFTEM is performed with a Zeiss 902 TEM (Oberkochen, FRG), connected to an image analyzer (IBAS, Kontron/Zeiss, Oberkochen, FRG) and a personal computer (Olivetti M280). In Figure 2, the spectral- and image-analysis chains are shown schematically in relation to the other control units of the microscope.

Instrumental details can be found elsewhere [6, 72-74, 79-82]. In short (see also Fig. 1), after the passage through the energy filter, the energy contents of the back-focal plane of the objective lens is projected as an energy-dispersed line in the energy-dispersive plane. In that plane, parts of the energy-dispersed line can be selected through the introduction of a slit. The slit width used for spectra acquisition is 1 eV, and for the acquisition of images is 10 or 15 eV. Spectra are acquired by irradiating an area in the specimen by a stationary beam of incident electrons. By changing the magnification, the size of this analyzed area can be varied from 7.5 nm^2 to 80 μm^2. The spectral information collected from that area is an average. Spectra are collected serially with the use of a photo multiplier tube (PMT), over an energy range of 100 eV before to 100 eV beyond the specific edge. During spectral acquisition each channel (width = 1 eV) is sampled with a dwell time per channel of about 500 ms. Spectral information per channel is stored 12 bit deep. To reduce noise, sometimes five spectra, recorded one after the other, are averaged. A quantitative spectrum analysis (QSA) module is used to extract the desired element-related net-intensity values.

In addition to the serially-recorded spectra by the PMT, parallel-recorded spectra can also be acquired [28, 36, 37]. From the energy-selective plane, about 70 eV wide, parts of the energy-dispersed line are projected in the TV-camera in the image-analysis chain to the IBAS. In this pathway, optical attenuation filters can be introduced such that the same gain, black level and kV settings of the camera can be maintained for the acquisition of parallel electron energy loss (PEEL) spectra in both the elemental-edge range and the zero- and low-loss range. In these images the corrections for dark current (I_{dark}) and shading (I_{shad}) of the gross-intensity image (I_{acq}), as proposed by Ross Messemer et al. [76], are incorporated. From the image of the energy-dispersed line, the intensities are acquired by data bunching (10 pixels $\approx$ 1 eV) along the line, and summation and averaging of pixels (1-21) perpendicular to that line. The final intensity is converted into a relative intensity versus energy-loss diagram. The IBAS is used to transfer this information to a personal computer for processing with curve-fitting modules. QSA-module used for the serially recorded spectra are applied to extract the desired $I_{K,L,M,N}$-values. In the image mode of the projector lens, energy information that passes the slit can also be projected as an image on the large screen or directed into a TV-camera by a small screen. This is called electron spectroscopic imaging (ESI). The energy-filtered images (and PEEL spectra) are recorded with a SIT-camera (Bosch, AEG, Amsterdam, Netherlands). Parts of the energy-dispersed line are isolated by the slit in the energy dispersive plane to allow image formation. All images are averaged 100 times and corrected for shading by subtracting an out-focus image. Some images acquired by ESI have been given specific names:

(**a**) zero-loss images, in which elastic- and inelastic-scattered electrons are excluded from the image formation and only zero-loss electrons pass the slit.

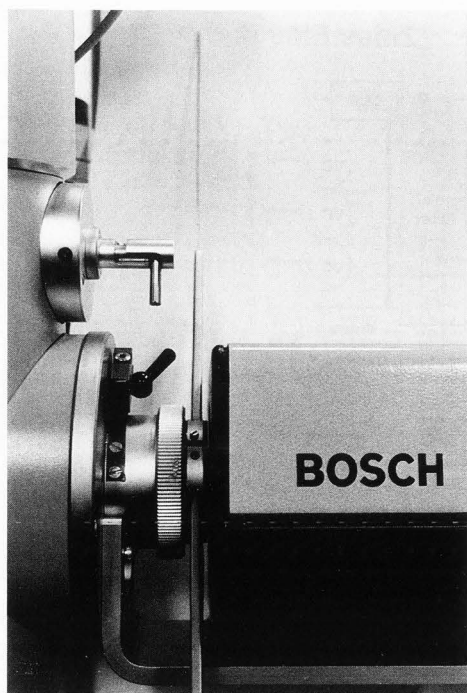(**b**) E_{250}-images, in which the contribution to the

Figure 3. Light-attenuation filter holder in the C-mount of the Bosch TV camera.

---

image formation of electrons derived from the element carbon is minimized, by placing the slit just before the carbon edge. As a consequence, all carbonaceous parts in the image are black, and sulphur and phosphorus containing parts are bright. Alternatively, parts with a high local mass will appear as bright in these so called darkfield images.

(**c**) Element-related images, in which electron information collected around ionization edges is included in the image formation. When spectral results have to be compared with results acquired in the image mode, decisions about slit-width, position and intervals between the images in the fitting zone (Γ zone), and the width of the integration zone (Δ zone) have to be taken. Moreover, it has to be realized that some results to be compared are acquired by two different electron detectors (PMT and TV camera). To minimize beam damage of the specimen, the acquisition of spectra and images is aided by a remote-control unit. In that case, the areas to be analyzed, are selected at very low beam intensities, and the x-y-coordinates of the area are stored. Then the beam conditions are optimized and subsequently all previously-stored sites are analyzed automatically one after the other in one run. The spectrometer settings are made manually. The data are stored on disk and are processed off-line.

The spectra and images are processed by quantitative spectral (QSA)- and image-analysis (QIA) modules [27, 81, 82]. The QSA module includes parts for objective ionization-edge identification and for curve fitting [27]. At each individual edge, first the actual position is accurately determined. Methods to acquire this position, and subsequently the edge identification, have been published [81, 82]. In short, the first or second derivative of the spectrum is used to find the proper position on the energy axis. The obtained eV value ($= E_{IE}$) is compared with a table which includes the known edge values from all elements. Energy-scale calibration, either using the position of the zero-loss or the carbon-edge, is applied to correct for observed offsets. Among the curve-fitting modules available: Simplex, steepest descent, log/log or linear, the Simplex method is used in most cases [8, 62, 64, 72, 84, 99].

In spectra, two ratios play an important role: R_x and R^*_x [82]:

$$R_x = I_{K,L,M,N} \, / \, (I_b + I_{K,L,M,N});$$
$$R^*_x = I_{K,L,M,N} \, / \, I_{(zero\text{-}loss \, + \, low\text{-}loss)}.$$

In those cases where the spectral R_x values have to be compared with those derived from images, the difference is indicated as ^sR_x and ^iR_x or $^sR^*_x$ and $^iR^*_x$ respectively. The R_x value, cannot be used for quantitative estimations, as the term $(I_b + I_{K,L,M,N})$ does not represent the total mass. The QIA-module includes fitting procedures for an assumed linear- and power-law relation and subtraction of the continuum portion of the digital images. In the resultant $(I_{K,L,M,N})$-image, grey values are objectively segmented and related to other image values. Calculation procedures are similar to those applied to spectral values. One of the problems related to quantitative EFTEM, is the difference in intensity between images acquired at the zero- and low-loss region, and those at the edges further away on the energy scale. These intensity differences may exceed the dynamic range of the recording system. As a solution to that problem, a new feature, the light-attenuation filter, is proposed which can be introduced in the optical path of the image chain (Fig. 3). Grey-filters (Kodak, Odijk, Netherlands), with a known optical density (O.D.), can bring the intensities present in the images (and parallel spectra) within the dynamic range of the TV camera.

The biological materials investigated are aldehyde-fixed cells or tissues (1.5 wt % glutaraldehyde in 0.1 M cacodylate/HCl buffer, pH 7.3). In cells, the concentration of endogenous elements, e.g., iron concentration in ferritin and siderosomes in liver parenchymal cells from biopsies from patients with an established hemochromatosis, are also investigated. Exogenous elements are introduced either prior to fixation or after aldehyde fixation by a cytochemical reaction [51, 82].

To aid in a Boron Neutron Capture Therapy program, experiments are performed in which a series of boron containing compounds are tested. The incorporation, presence, and possibly the concentration of intracellular boron are investigated by EELS analysis. Inside pre-melanosomes, the presence of intra-cellular boron is shown after 24 hour cultivation of melanotic B16 murine melanoma cells with borocaptate sodium [95].
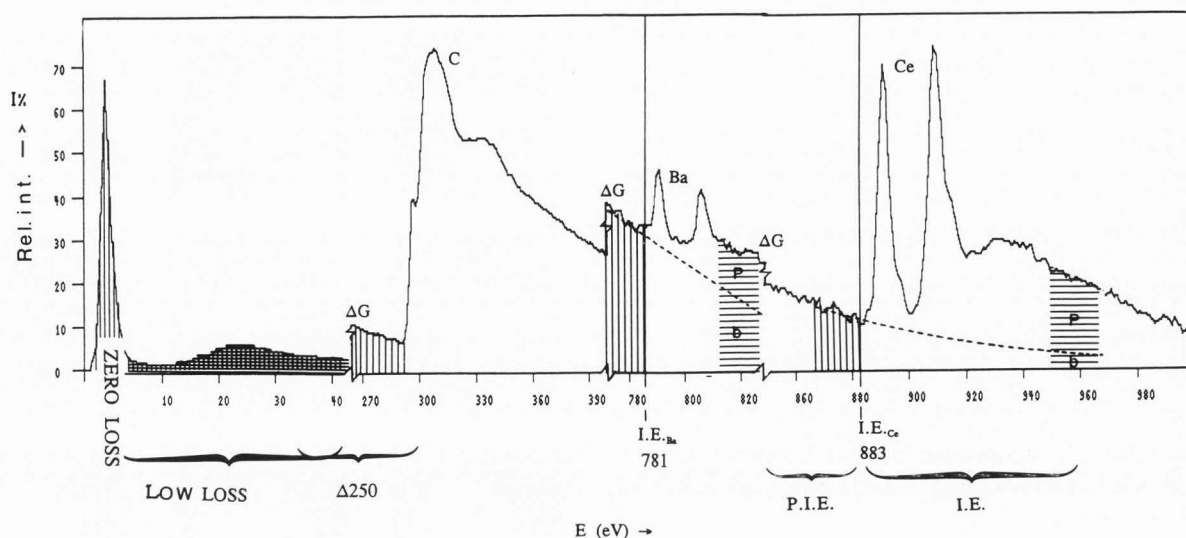
Figure 4. A compiled spectrum including the zero- and low-loss region, and the C, Ba and Ce edges.

To aid in investigations concerning kidney-stone formation, polarly cultured tubule lining cells were challenged with oxalate. The presence of calcium is detected in calcium oxalate monohydrate (COM) crystals inside polarly-cultured $LLCPK_1$-cells. Intracellular crystals are acquired after a 24 hour oxalate load at the apical side of the cells with 500 μMol lithium oxalate in complete medium. In all cases, the aldehyde-fixed cells or tissues are dehydrated in graded ethanol or acetone series and epon embedded. Wet-sectioned, unstained, ultrathin sections, collected on bare 400 mesh copper grids, are used for analysis.

Bio-standards with known externally determined element concentrations, are used for spectral- and image quantification. Bio-standards are Chelex[100]-based ion-exchange beads or particles with a diameter between 50-75 μm into which cations are immobilized. Bio-standards are commercially available from Bio-Rad (Veenendaal, Netherlands). The mean concentration of the elements is determined by neutron activation analysis. The specific mass of these beads is determined by measuring the mean volume from a weighted amount of beads, with the aid of a Coulter Counter Multisizer II (General Electric, Coulter Div., Luton, U.K.). The beads can be co-embedded with the tissue containing the "unknown" concentration of the same element. Because the unknown and the Bio-standard with the known concentration of the element are present next to each other in the same section, both sites were assumed to have the same section thickness [9, 10, 18-24, 63, 94]. Both sites are included in the same run of the remote-control program.

Bio-standards are also used as test-objects for instrumental-parameter control. Because the mean concentration of the Bio-standards is constant, their mean R_x values are constant. This fact can be used to monitor the influences of instrumental parameters or computation procedures. The presence of the energy filter is also used for contrast-sensitive imaging of thick (1-3 μm) epoxy sections [44, 45, 66, 68, 91].

Morphometric analysis has been applied to all three types of images and proceeds along the same lines. Grey-value frequency histograms are obtained from the digital, shading-corrected images. In these histograms, the contribution of each population (embedding medium, cytoplasm, nucleus, particles or lysosomes) is objectively separated, making use of the first derivative of the histogram. Other segmentation procedures can also be applied [93]. Following this segmentation step, the relative area occupied by each population is determined by counting the pixels in the various segments. Subsequently, making use of conventional EM magnification-calibration methods, the area in pixels is converted to the area in nm^2 or μm^2. It has been shown [79, 80] that the area of colloidal gold and thorium particles, measuring about 1-2 nm in diameter, can reliably be segmented and measured.

Results

Quantitative spectral analysis (QSA)

Serial EEL-spectra. Figure 4 shows an extended spectrum including both the zero-loss and part of the low-loss region. The carbon edge (at 284 eV), the barium edge (at 781 eV), and the cerium edge (at 883 eV) are visible as ridges on a steadily decreasing continuum. In Figure 4, ΔG indicates the steps in the PMT-gain introduced to bridge the intensity differences. In our PMT-spectral acquisition line, these steps are manually switched amplifiers. The continuum is assumed to follow a power law as a function of energy loss:

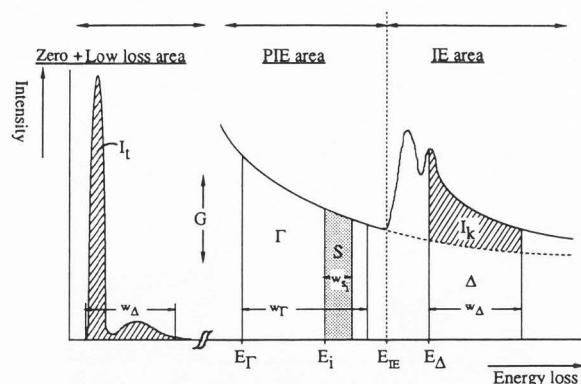$$I(E) = A * E^{-r} \qquad (1)$$

697

Figure 5. Relation between the spectral fitting- and integration zones and the images, acquired with a given slit (S) of width ($W_{s,i}$) both in the edge- and the zero-loss plus low-loss region.
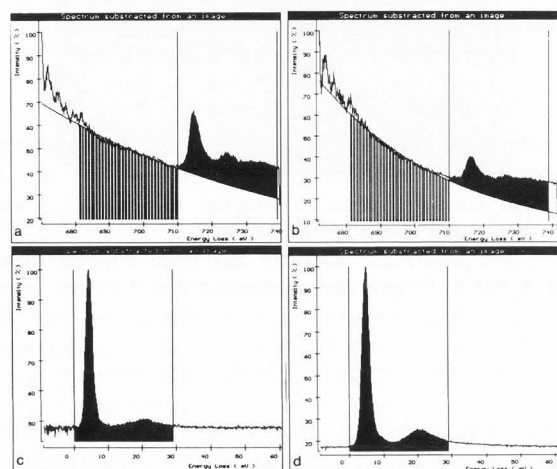

Figure 6. Parallel EEL spectra. (**a**) A [P]EELS iron spectrum from an iron containing lysosome (siderosome). (**b**) A [P]EEL spectrum of an iron containing Bio-standard. The (30 eV wide) Γ-regions for exponential fitting and extrapolation for subtraction of the continuum beyond the edge, are hatched. The vertical bars indicate the Δ-region of 30 eV. (**c**) The intensity reduced [P]EEL spectrum (corresponding to Fig. 6a) of the $[E_{(zl+ll)}]$ region, with an optical filter installed (O.D. = 5), from the siderosomal area. (**d**) Similar [P]EEL spectrum of $[E_{(zl+ll)}]$ region from the Bio-standard's area corresponding to Fig. 6b.

The zones around the E_{IE}'s are divided in pre-ionization (PIE) and ionization edge (IE) areas. In the PIE area, a zone (called Γ-range) with a width of 100 or 50 eV, is used to estimate the values A and r in eq. 1 using a curve-fitting model mostly based on a least squares approach or a maximum-likelihood procedure based on Poisson statistics [92]. The accuracy and precision of these methods are extensively discussed and compared [5, 8, 13, 14, 16, 35, 37, 54-58, 60, 69, 70, 78, 85-88,
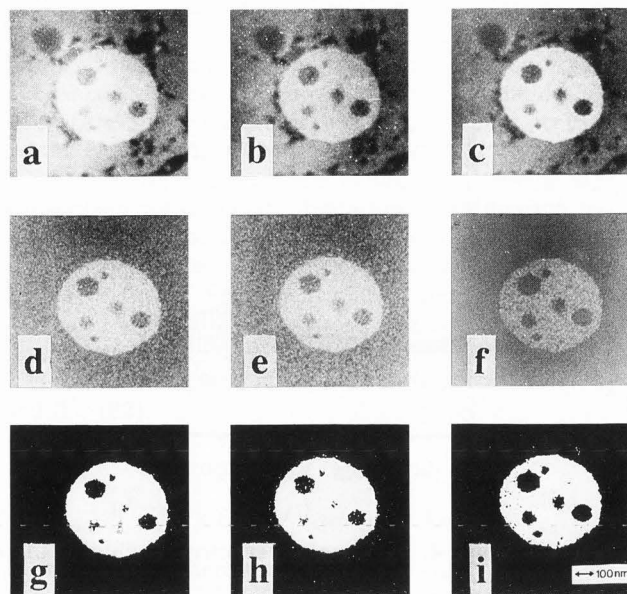

Figures 7a-i. This series of images show the consequence of the choice of fitting procedure upon the area occupied by the net-intensity of the element. Figures **7a** and **7b** show two pre-edge images (648 eV and 688 eV), while Figure **7c** shows the Fe gross-intensity image at 728 eV. The images in Figures **7d-f** are the Fe net-intensity images and in Figures **7g-i** their binary Fe net-intensity images. Figures **7d** and **7g** are acquired after application of a power-law fitting method, Figures **7e** and **7h** after a linear fitting method, and Figures **7f** and **7i** after application of the two window method.

92, 97, 101]. Once the values of A and r have been obtained, they are used to extrapolate the continuum to the region beyond the E_{IE}. This allows one to determine the $I_{K,L,M,N}$-value over the Δ-range by subtracting the continuum component. When this value is related to the zero- plus low-loss intensity (I_{zl+ll}), representing the total mass of the irradiated analyzed area, the relative element concentration can be estimated. When related to the net-intensity values from other elements present in the same irradiated area, elemental ratios can be obtained.

In Figure 4, areas are marked by vertical and horizontal lines, from about 15 eV wide, which indicate spectral zones from which images can be acquired through the introduction of the slit. In Figure 5, this situation is exemplified. In the PIE area, a Γ-range, with a width of 100 or 50 eV (W_Γ), is indicated. This zone is sampled by a slit (S) with slit-width ($\Delta_{s,i}$), used to estimate the values of A and -r in eq. 1. The same curve-fitting models, based on least squares approaches or a maximum-likelihood Poisson statistical procedures, are used for images. Other methods using linear extrapolation and a two-window method have also been proposed [35]. After subtraction of the calculated I_b-image,

Table 1. Area$_{Fe}$ fractions and R$_{Fe}$ values from the same image (present in Fig. 7), after a two window (PIE), a linear- (LIN), and power-law (Log) fitting procedure.

	PIE		Lin		Log		$^{S}R_{x}$
	$^{I}R_{x}$	A (μm^2)	$^{I}R_{x}$	A (μm^2)	$^{I}R_{x}$	A (μm^2)	
E$_{\Delta 1}$ (713 eV)	0.10	1.539	0.16	1.580	0.13	1.457	0.41
E$_{\Delta 2}$ (728 eV)	0.17	1.569	0.20	1.577	0.19	1.567	0.35
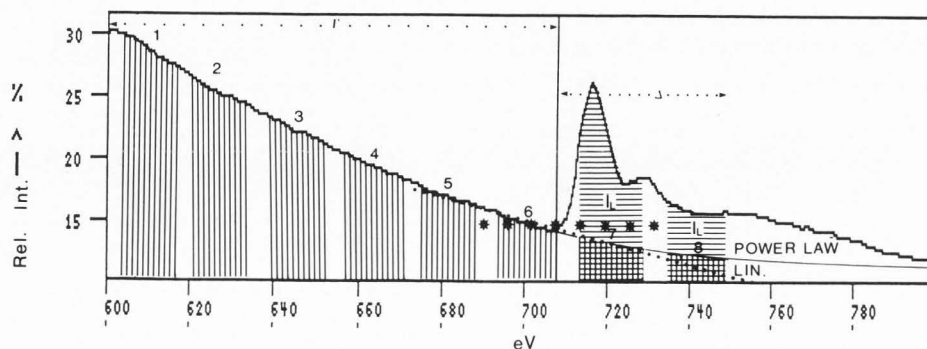
Figure 7k. The relation of the slit positions for the images in a spectrum and the three fitting procedures is shown schematically.

---

the element's net-intensity (I_K)-image is obtained. Similarly, several images in the Δ-range beyond the edge have to be acquired. In Figure 5, the position of the Δ-zone is deliberately not chosen at the onset of the edge to indicate that the optimum for this position and the width of this zone (w$_\Delta$) has to be established. When these I_K-image(s) are related to the zero- plus low-loss intensity (I_{zl+ll})-images, representing the total mass of the irradiated analyzed area, relative element-concentration images can be obtained. For estimation of the continuum beyond the edge: $W_\Gamma \approx W_\Delta$. For concentration calculations: $W_\Delta(I_K) = W_\Delta(I_{zl+ll})$. In both cases, several images have to interrelated and/or added. The fitting and calculation procedures have to be applied to each pixel in the (512^2) images.

Parallel EEL (^{P}EEL) spectra. The application of the calibrated attenuation filters to acquire intensity-reduced ^{P}EEL spectra from the zero-loss plus low-loss [E$_{(zl+ll)}$] region for an iron-containing lysosome (siderosome) and an iron-containing Bio-standard (for an explanation of the use of Bio-standards, see below) is shown in Figures 6a-d. Manipulation of these spectra by application of the QSA-module resulted in a spectral $^PR*_{Fe}$ value. In Figures 6a and b, the fitting procedure applied is the log/log method. True $^PR*_{Fe}$-values, integrated over 30 eV, are: 4.314x10^{-6} for the siderosome and 2.613x10^{-6} for the iron Bio-standard. The final iron concentration in the analyzed area of this siderosome is calculated according to:

$$N_{sid} = R^{*}_{sid} / R^{*}_{st} \cdot N_{st} \qquad (2)$$

When, e.g., N$_{st}$ = 1800 Fe atoms, this will result in 2971 iron atoms to be present.

Quantitative image analysis (QIA)

Image analysis will be divided in two parts: (a). segmentation and morphometry of contrast-sensitive and element-related images, and (b) acquisition and analysis of elemental net-intensity images.

Morphometric analysis. Image segmentation and morphometry are rather important image processing steps that allow both structural and compositional image analysis from heteromorphic objects in the cells. For structure analysis, zero-loss and E$_{250}$-images, are used as contrast-sensitive images, to which element-related images from the compositional analysis are related by superposition of two images. A protocol for objective segmentation of items of interest in such images has been proposed before [80].

Acquisition and analysis of elemental net-intensity images. The same procedures, as applied to spectra have to be applied to a series of images acquired around the E$_{IE}$.

To demonstrate that $^{I}R_{Fe}$ values can be acquired and $^{I}R_{Fe}$ and $^{S}R_{Fe}$ can be compared, cross-sectioned Bio-standards were analyzed. The mean $^{I}R_{Fe}$ value is: 0.21, the coefficient of variance (CV) = $\pm$ 17% (acquired by the image mode/TV chain, slit width 15 eV, linear fitting mode, n = 6) from an analyzed area (1.60 μm^2) and for W$_\Delta$ = 15 eV. This value differs from the mean $^{S}R_{Fe}$ value: 0.14, CV = $\pm$ 7% (n = 6), acquired under similar conditions by the spectrum mode/PMT chain and 1 eV/channel. However, the interval between the individual values is constant. It is realized that the applied fitting procedure will influence the final result. These effects were investigated. The results are shown in

Figure 7. Figure 7k, shows schematically, the slit positions around the IE_{Fe} used in our experiments. Previously, one pre-ionization-edge image was subtracted from the ionization-edge image, the so called two window method (Fig. 7k, image 7 minus image 6). This method underestimates the element net-intensity portion. More accurate is the linear fitting method, which may overestimate the element net-intensity portion when the continuum is subtracted. The best method is considered a fitting procedure that follows a power-law model. Both methods assume a relation (linear, power law) between the image-intensities in the continuum of the Γ-range, which is used, for each pixel in the image, to calculate the extrapolated continuum portion in the image(s) beyond the E_{IE}. This extrapolated portion is subtracted, pixel by pixel, from the image(s) beyond the edge, to give the net-intensity image, which can be made binary (iron containing sites white, remainder black).

In Figures 7a-i, as detailed in the figure legend, the consequences of the choice of the fitting procedure upon the area occupied by the net-intensity of the element are shown. These images are acquired from a siderosome. The white, iron containing area in Figure 7i is smaller than in Figure 7g; whereas, the iron-containing area in Figure 7h is larger than in Figure 7g. From the images shown in Figures 7g-i, the area fractions and R_x values are calculated.

Table 1 shows the results of these calculations following objective segmentation. The influences of fitting procedures upon the calculated $^I R_{Fe}$ values and Fe-areas confirm the observations shown in Figures 7g-i. The changes observed in the $^I R_{Fe}$ values confirm that the position of the slit in the Δ-zone influences the calculated $^I R_x$ value, as suggested in Figure 7k. The $^I R_{Fe}$ values are compared to the same ratio in the serial spectrum from the same area ($^S R_{Fe}$).

To illustrate the practical application of the QIA procedure, two examples are given. The possibilities of compositional EELS analysis by images is shown in Figures 8a-c. The combination of compositional and structural analysis is shown in Figures 9a-c.

QIA-procedure applied to calcium detection. The presence of calcium, intracellularly located in calcium oxalate monohydrate crystals in cultured $LLCPK_1$-cells, is shown in Figure 8. A power-law relation over a rather short Γ-range ($W_\Gamma = 30$ eV) is assumed to be present among the pre-ionization edge images ($W_\Delta = 15$ eV).

QIA-procedure applied to boron detection. In Figure 9a, a contrast-sensitive E_{250} eV image of melanosomes-containing cells is shown. The presence of boron in such melanosomes is established by qualitative spectral analysis (not shown). In Figure 9b, the boron gross-intensity image is shown. In Figure 9c, the acquired boron net-intensity image is shown after a linear fitting model of three Γ-range images (not shown). The visibility of the cellular components of the image has disappeared. In Figure 9d, the boron net-intensity image in Figure 9c is superimposed over Figure 9a. The presence

Figure 8. (a). The contrast-sensitive E_{250} eV image (at low magnification) of intracellularly located Ca in calcium oxalate monohydrate crystals in cultured $LLCPK_1$-cell after an apical oxalate load. (b) One of the calcium pre-ionization edge images from the crystals. (c) Calcium net-intensity distribution image (after a norm grey intensity stretch). Power-law fitting over a rather short Γ-range and extrapolation. (d) Binary calcium net-intensity distribution image, all calcium containing parts are in white. Bars = 15 μm (in a) and 4 μm (in b; c and d show the same area as in b).

----

of boron is indicated by the black central part of the melanosomes. Among the set of melanosomes present in Figure 9c, some have incorporated boron while others have not.

Concentration-distribution images

In the next image acquisition experiments, the number of images is increased, and an attenuation filter is introduced in the optical path to the TV camera. Our images were taken below the iron edge (at 628, 648, 668, 688 eV) and two beyond the iron edge (at 718 and 738 eV) without a filter. Subsequently, with an optical filter (O.D. = 5) introduced, one image each in the $E_{(zl)}$ region (0-15 eV) and the low-loss region (15-30 eV) is acquired with the same camera-gain. Off-line application of a linear fitting procedure to the images below the E_{Fe} edge position resulted, after extrapolation, in the iron I_L net-intensity images. All pixel values in the "optical-filtered" $E_{(zl)}$-image are multiplied by 10^5, representing (partially) the total mass of the irradiated area (= I_T-image). The $^I R^*_{Fe}$-image is now calculated by $I_L/(I_T)$. This set of images is shown in Figure 10 for a siderosome.

The use of Bio-standards in the quantification process

The use of Bio-standards with a known (externally determined) immobilized element concentration, present in an organic matrix more or less similar to the cellular matrix, has become common practice, e.g., in X-ray-microanalysis [7, 9, 10, 18-25, 27, 63, 75, 80]. Use of similar Bio-standards as test specimens for a variety of EELS-related aspects [26, 27] and for the quantification of biological specimens with EELS analysis [81-83] has been proposed.

The use of Bio-standards in EELS may be theoretically justified as follows: denoting the number of atoms of element x per unit area by N_x, the total number of atoms per unit area by N_T, and the atomic concentration of element x by C_x:

$$N_x = C_x * N_T = C_x * \{(N_A * \rho)/A\} * t \qquad (3)$$

where N_A is Avogadro's number, ρ is the physical density, A is the atomic mass, and t = the section thickness. In a binary system, e.g., when the concentration of iron in pure carbon is required, ρ_C and A_C are known. In biological systems, the cell matrix is composed of various elements (C, H, O, N, P, S) which may vary rather
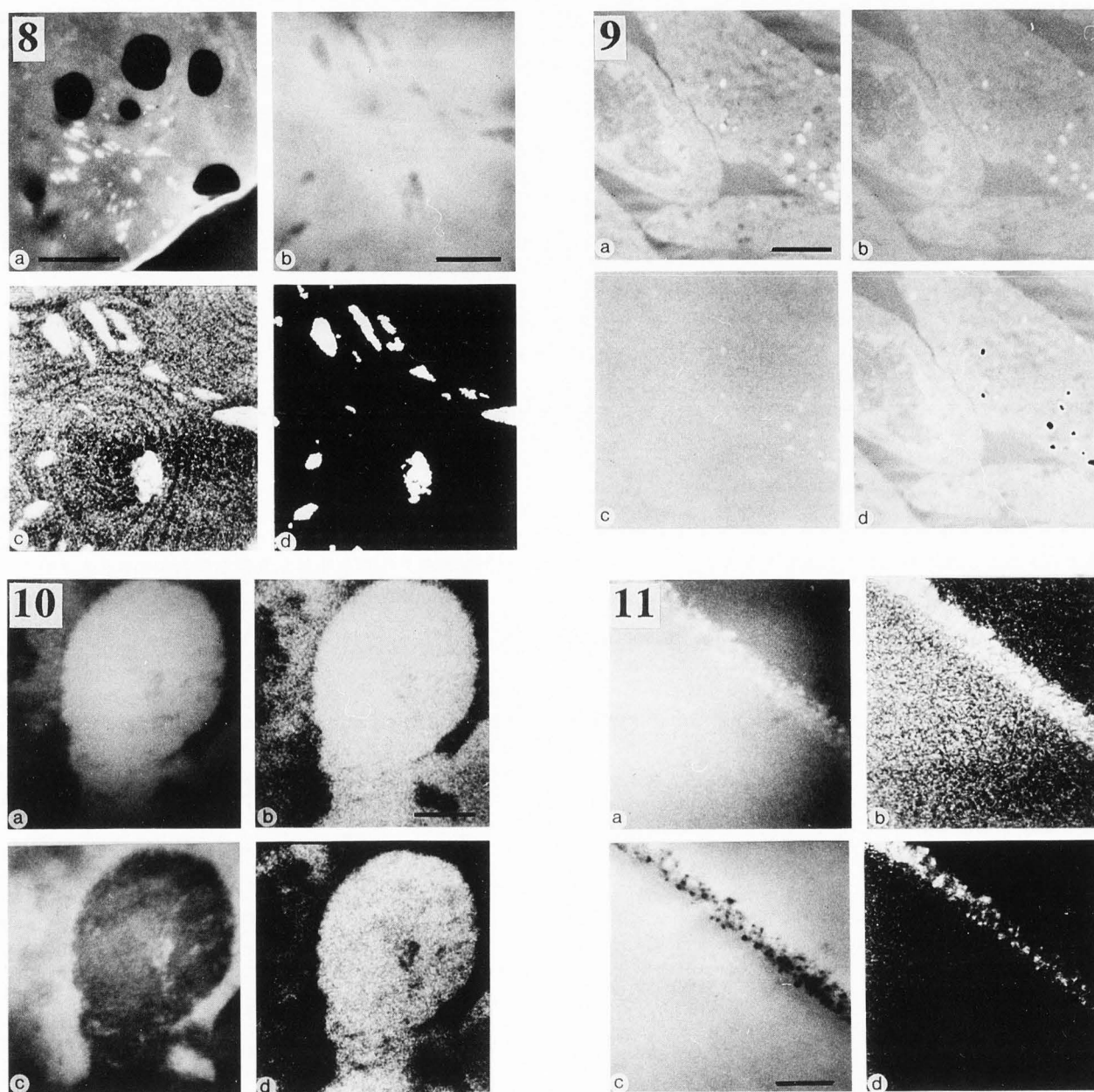
Figure 9. **(a).** The contrast-sensitive E_{250} eV image of melanosomes containing cells. **(b).** The boron gross-intensity image. **(c)** The boron net-intensity images acquired following a linear fitting of three Γ-range images and extrapolation. **(d).** The boron net-intensity image of Fig. 9c is superimposed over Fig. 9a. The melanosomes that do contain boron are black. Bar = 10 μm. (all four images at same magnification).

Figure 10. **(a)** Gross Fe-image. **(b)** Fe I_L net-intensity image, derived from Fig. 10a after linear fitting of 4 pre-ionization edge images (not shown) and extrapolation. For representation the contrast is stretched (norm grey). **(c)** "Optical-filtered" $E_{(zl)}$ image (O.D. = 5 filter). **(d)** Resultant $^I R^*_{Fe}$-image (W_Δ = 15 eV). Bar = 200 nm (all four images at same magnification).

Figure 11. **(a)** Fe gross-intensity image of a Fe-containing Bio-standard. **(b)** Fe net-intensity (I_L) image derived from Fig. 11a after linear fitting of 4 pre-ionization edge images (not shown) and extrapolation. **(c)** Zero-loss "optical-filtered" $E_{(zl)}$ image taken with an O.D. = 5 filter. **(d)** Resultant $^I R^*_{Fe}$ image (W_Δ = 15 eV). Note the higher iron concentration at the bead's rim. Bar = 200 nm (all four images at same magnification).

Table 2. Area fractions (in pixel %) of the cytoplasm/Epon and the three discriminated iron ([Fe]) concentrations (shown in Fig. 12b as white, grey and dark grey), and those of the iron concentration distribution images of 718 eV/ zero-loss and 738 eV/zero-loss from the same siderosome.

Image	Object	Cytoplasm/EPON	$[Fe_1]$	$[Fe_2]$	$[Fe_3]$
718 eV/Zero-loss	Siderosome	16.3	61.4	22.2	0.1
	Standard	90.7	8.7	0.4	0.2
738 eV/Zero-loss	Siderosome	11.1	40.4	46.2	2.3
	Standard	69.9	27.6	1.9	0.6
718+738 eV/Zero-loss + low-loss	Siderosome	8.9	37.4	49.2	4.5
	Standard	74.8	23.2	1.4	0.6

drastically in local composition, this matrix composition is unknown and the mean A and ρ have to be estimated as accurately as possible.

At a particular edge ($E_{K,L,M,N}$), the net-intensity signal I_x, due to the presence of element x, is related to N_x through the expression:

$$I_x(\beta, \Delta) = N_x \cdot I_T(\beta, \Delta) * \sigma_x \qquad (4)$$

In eq. 4, σ_x is the partial cross-section of element x. It expresses the probability that an incident electron interacts with the element x and will create the particular edge phenomenon. The constants β and Δ are instrumental parameters; I_T is the total intensity. When a second element y is present in the same irradiated volume, and its intensity contribution is acquired in the same spectrum, I_y is similarly expressed as:

$$I_y(\beta, \Delta) = N_y * I_T(\beta, \Delta) * \sigma_y \qquad (5)$$

When it is sufficient to know the ratio of the concentrations of element x to y, than:

$$(N_x * \sigma_x)/(N_y * \sigma_y) = I_x/I_y \qquad (6)$$

thus, the I_T value is eliminated and the ratio of concentrations of elements x and y is independent of A and ρ. Theoretical considerations of the σ-values can be found in the literature [56]; computer programs are available to estimate the various σ values [see 35]. It has been reported however, that the theoretically expected ratio (eq. 6) may not be observed due to differences in sensitivity of the two elements for beam damage [30].

When, in one ultrathin section, an element (x) is present in an unknown concentration at one site (1) and as a known concentration in the Bio-standard in a second site (2), element net-intensities may be related to each other. Provided it may be assumed that: a) $\sigma_{x1} = \sigma_{x2}$, (b) $t_{x1} = t_{x2}$ and (c) $N_{x1} \approx N_{x2}$, the following relationship holds:

$$N_{x1} / N_{x2} = (I_{x1}/I_{T1}) / (I_{x2}/I_{T2}) \qquad (7)$$

When N_{x1} is much different from N_{x2}, a correction procedure has to be applied [9, 10]. In previous papers [81, 82] the ratios in eq. 7 have been indicated as R^*_x-values:

$$N_{x1} / N_{x2} = R^*_{x1} / R^*_{x2} \qquad (8)$$

When, as assumed above, N_{x2} is the known concentration, then:

$$N_{x1} = (R^*_{x1} / R^*_{x2}) * N_{x2} \qquad (9)$$

In practice, (N_{x2}/R^*_{x2}) may be replaced by one single factor, f; because previously it turned out that the mean R^*_{x2} ratio, acquired from several Bio-standard cross-sections was, within limits, rather constant [10, 24].

Segmentation of the iron concentration-distribution image. In Figures 11a-d, a set of images of a Fe-Bio-standard is shown, these corresponds to the acquisition of the siderosomal set shown in Figures 10a-d. When the grey values in Figure 11d are objectively segmented, the mean grey value, representing the "known" iron concentration, is obtained. Similarly, the siderosomal iron-concentration image (Fig. 10d) is segmented, separating the iron-containing sites from the cytoplasm. The remaining iron-related grey values can be scaled in multiples of this mean Bio-standard value. The resultant concentration classes are each given a false color or, are given different grey tones in the print. The area fraction of each of these concentration zones can be calculated. In this way, the influence of the attenuation filter is nullified in this calculation. The results shown in Figure 12 are from the same acquisition run as shown in Figures 10 and 11. In Figures 12a,b, the W_Δ is increased to 30 eV, by adding two iron net-intensity images (718 + 738 eV) to get one I_L-image, which was subsequently divided by two added images from the zero-loss region (I_{zl+ll}). In Figure 12b, segmentation in three-iron concentration classes is shown. In Table 2, the calculated areas of the three classes are given ($[Fe_1]$-$[Fe_3]$; $[Fe_3] > [Fe_2] > [Fe_1]$). Moreover, according to expectation, the multiplicative shading present in the added images is removed by dividing the two added images by the added zero-loss plus low-loss image, to obtain the $^IR^*_{Fe}$-image.

Discussion

The instrumentation for EELS has proceeded to a level where both structural- and compositional analyses of biological entities can be performed adequately. Reliable, *in situ* acquired, qualitative information about the chemical elements in defined morphological structures can be obtained from cells and tissues. The introduction
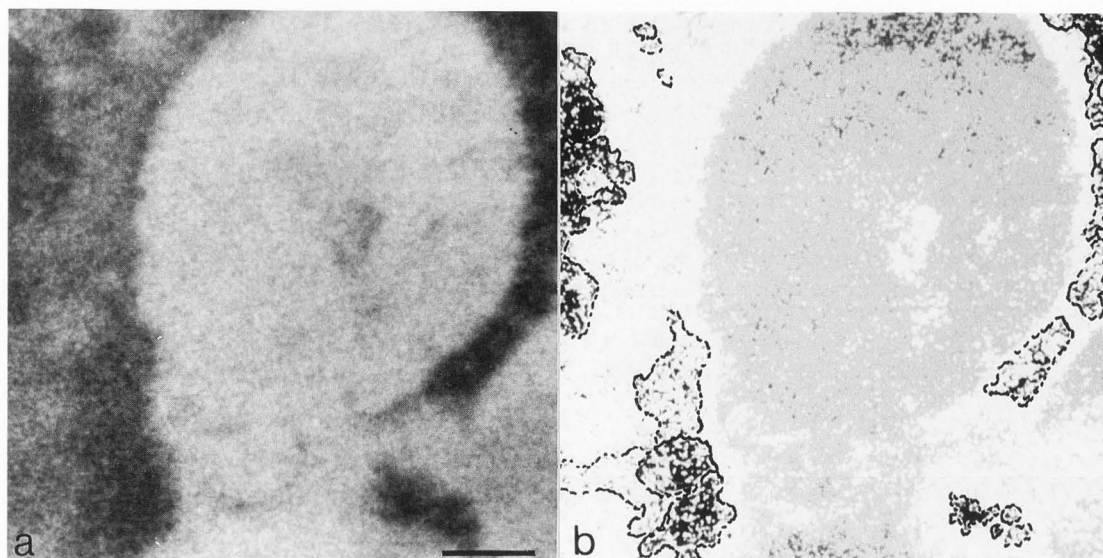
Figure 12. (a) Iron concentration image similar to Fig. (10d); the Δ-range is increased to 30 eV (718 + 738 eV divided by the zero-loss plus low-loss images). (b) Iron-concentration segmentation image of Fig. 12a. Segmentation, based upon the mean grey-value of the Fe-Bio-standard into three classes (white, mainly the ferritin outside the siderosome, light grey and dark grey inside the siderosome, cytoplasm = black).

----

of TV-and CCD-cameras coupled to powerful computers allow spectra and images to be extracted from the microscope for further, digital quantitative processing. The part of off-line computer-assisted spectrum manipulation and image reconstruction has become increasingly important and time consuming. Consequently, the mathematical processing of the digital information in spectra and images is now dominating the final result to a large extent. The old adage about absence or presence of items of interest or (reaction) products: "seeing is believing" has been replaced by concepts like: signal to noise ratio and precision and accuracy.

By the combination of EEL spectral- and ESI-analysis, the early claims [1-4, 42, 43, 65] about the high spatial resolution of the element information have been confirmed [12, 15, 28, 80, 83]. For small particles with a high local concentration (colloidal gold = 100 wt% Au; colloidal thorium oxide = ~88 wt% Th; ferritin = ~30 wt% Fe), reliable structural measurements in images can be performed, after objective segmentation. A spatial "resolution" of 1-2 nm, with a reasonable precision (coefficient of variance = 20%) and with 25-50 pixels per particle can be obtained. However, 50 pixels/particle is too low a number for accurate area measurements [100]. Improvement of the accuracy by increasing the number of pixels per frame from 512^2 to 2048^2 will, for such small particles, be feasible though marginal. The improvement will be appreciable for particle diameters over 10 nm [100].

The compositional analysis suffers somewhat more from inaccuracy and imprecision. The main problem is to bridge, during spectral and image acquisition, the differences in the intensity range between the elemental- and $E_{(zl+ll)}$ region. The proposed introduction of calibrated attenuation filters in the optical path to the TV-camera overcomes this practical problem. It allows the acquisition of images and spectra in the $[E_{(zl+ll)}]$ region with the same camera-gain setting as the one required for the edges. It is expected that the use of the attenuation filters will improve the precision of the analyses. It is realized, that the type of PEELS analysis with a TV-camera is a "poor man's solution" as compared to the genuine 1024 diode array detector, but: (1) the same detector may be used for images as well as for spectra, (2) it allows one to install in the C-mount connector the optical filter set, and (3) in that way the dynamic intensity-range restrictions can be bridged.

In this review, we have tried to bridge the gap between quantitative spectral- and image analysis, to some extent related to the instrumental conditions present in the Zeiss EM 902. Theoretically, both results have to be the same but practical differences may occur. Our results are shown in Figures 6-12. Initially, using the attenuation filters for the iron PEELS spectra, the spectral values (I_{corr}) have been obtained by the application of an equation proposed by Ross-Messemer et al. [76].

$$I_{corr} = [(I_{acq} - I_{dark}) / (I_{shad} - I_{dark})] * f \qquad (10)$$

Later it turned out that in our case, with the use of the camera light controller, the image for the shading correction (=I_{shad}) and the dark current image (=I_{dark}) of the iron region were virtually identical and did not contribute to the correction of the I_{acq} Fe-intensity images.

For the acquisition of the I_{zl+ll} image values, corrected for the I_{shad} acquired under the same condition with the optical filter, the spectrum includes a part before the 0 eV region. This portion contains the I_{dark} contribution, and has been subtracted from the whole spectrum. Although, it turned out that the shading of the images was nullified, the shading of the ^{P}EELS spectra is still a problem, not completely solved. The usual option for additive shading, applicable for images, by the subtraction of an out-focus image, did not work for the rather intense images from the energy-dispersed line. We used a slight lateral translation of the energy-dispersed line on the TV screen. Inaccuracies, in the acquisition of the parallel spectra have a great influence on the outcome of the fitting procedure. We have not yet completely mastered the noise, present in the lateral aspect of the spectrum (= perpendicular to the energy-scale direction).

In Figure 8, the presence of calcium, in calcium oxalate monohydrate (COM) crystals inside polarly-cultured proximal tubule cells (LLCPK$_1$) is shown after an oxalate load at the apical side of the cells. Previously, we have tried to estimate the calcium concentration of such calcium oxalate monohydrate crystals observed inside rat proximal-tubule cells after an oxalate-stone-inducing diet [82]. The acquired concentration values were close (-3 to +5 wt%) to the theoretical calcium fraction in such crystals. However, the standard deviation was rather large, due to the high beam sensitivity of such crystals. The use of the optical filter might improve the results in future.

In Figure 9, a set of images is shown demonstrating the relative boron concentration in melanosomes in B16 cells co-cultivated for 24 hours with borocaptate sodium. However, a reliable boron Bio-standard is not yet available, so the bias cannot yet be estimated. In this set, we showed the possibility of the combination of structural and compositional images. In Figure 9c, boron positive- and negative melanosomes are present. Some boron positive melanosomes with a low concentration, present in Figure 9c, are not indicated as such in Figure 9d. The additional segmentation procedure to create the overlay, shown in Figure 9d, causes some positive melanosomes to be excluded, as their grey value differs only slightly from the mean background level. The fitting procedure for boron spectra below 188 eV is rather complicated. But, the observation that in similar cell organelles, 24 hour-incubations with several other boronated compounds do not give net-intensity boron images, convinced us that true boron is visualized and hence incorporated. Moreover, we noticed that the organic boron compounds are rather beam sensitive and are easily removed during observation. On the other hand, power-law-fitting procedures were less convincing in the demonstration of boron in the boron-positive marked particles in spite of clear edges in the spectra.

The use of Bio-standards is advocated for the estimation of the bias of the analyses. Usually, the element concentrations of the Bio-standards, as determined by neutron activation analysis (NAA), are given in weight percent rather than as atomic concentrations, so a conversion must be applied. For that purpose, the ρ and the mean A of the matrix of the Bio-standards have to be determined. Procedures to acquire these values have been described [21, 22, 75, 82]. A prerequisite for accurate analyses is the homogeneity of the element distribution, both within one cross-sectioned Bio-standard and between the various Bio-standard cross-sections. The presence of an outer rim with a higher iron concentration than the mean concentration inside is not a common observation. It has been shown [7, 21] with the use of X-ray microanalysis, that the intra- and inter-bead variation is the same and between 15-20%. As a consequence, this Fe standard is certainly not ideal. So, several acquisitions from the Bio-standards have to be made to obtain a reliable mean value for R^*_{x2}. The use of the Bio-standards, as a way to estimate the bias in the acquired quantification procedures, assumes a linear relation between the standard and the unknown. This might not always be the case.

The experiments in which the mean $^IR_{Fe}$ is compared with the mean $^SR_{Fe}$ value were performed to assure that such $^IR_{Fe}$ value could replace the $^SR_{Fe}$ value. It demonstrates the use of Bio-standards as a calibration aid. The differences between the two values might be caused by the differences in their acquisition by the PMT or TV camera. Initially we had the idea to find, in the Δ-region, a ^IR_x value that could be used as a substitute for the serially acquired spectral value from that area. However, this idea was abandoned, when later results showed that net-intensity images could be added, to increase the Δ-range. An obvious conclusion from our experiments, shown in Figures 7a-k, is that the fitting procedure do influence the final result, and only the exponential fitting procedure gives the correct answer, for the compositional image analysis, in spite of the rather complex image computation.

Another aspect is the measurement of the section thickness t, and the mean free-path. We assumed here that: $t_{x1} = t_{x2}$, which still has to be demonstrated. It has been shown that the mean free path (λ) for the embedding medium epon is about 112-118 nm, for 80-100 keV electrons [35, 54, 55, 61, 70, 71]. Recently, Door *et al.* [29] measured λ-values for epon that deviated by about a factor of 2 from the calculated values (λ_{epon} = 208 $\pm$ 3.2 nm). We obtained, by re-embedding of (electron-optically) measured sections, a similar value for our epon medium (λ_{epon} = 209.1 nm). This aspect has to be further investigated, because section thicknesses calculated with the λ_{epon} = 112-118 nm are unrealistically low [82].

Quantitative EELS analyses through ESI can be performed and will result in true concentration-distribution images. In such images both the area occupied and the concentration in that area can be determined. The application of the attenuation filters in the optical path to the TV camera aids in the acquisition of reliable zero-loss and low-loss images (and spectral values in ^{P}EELS spectra). The presence of cross-sectioned Bio-standards

with a known externally determined concentration aids in the determination of the bias in the analyses. The minimum number of images in the pre-edge region for a adequate fitting still has to be established. In practice, there is no limitation of the number of images needed for the width of the Δ-range, as addition of images can be performed. In both cases, the criteria valid for spectra have to be applied for the images. Initially we have chosen the intervals between the images about 5 eV larger than the slit width, to prevent overlap. Later it turned out that when the slit width is carefully calibrated, this margin can be reduced to 1-2 eV. We did not investigate the influence of the slit width in great detail. Reduction below 10 eV is possible but interferes with the "exposure time" when images around edges, far away from the zero-loss zone, have to be recorded. In principle, a rather high number of 3-5 eV-wide images may be used to reconstruct parallel EELS spectra (image-based EELS). There is a change in the area fractions and in the iron concentrations when the three iron-concentration images are objectively segmented (Table 2). It remains to be proven, that the values acquired with a Δ-range of 30 eV, are to be preferred. The duration of the image processing as compared to the duration of the spectrum processing is at present rather long (hours versus minutes) which favors the latter. However, when the duration of the processing can be reduced, EELS analysis by ESI might be an alternative for heterogeneous objects in cells and tissues.

In addition to the instrumental improvements, two new aspects deserve attention: (1) Recently, Bonnet, Trebbia and coworkers [89, 90] proposed an alternative method for continuum "correction" in ESI. This new method is non-parametric in a way, that it does not assume any parametric form of the behaviour of the continuum. The method uses the formalism of correspondence analysis [38, 39, 89, 90]. Very recently, Gelsema et al. [38, 39] have proceeded along that line to explore the merits of this method for quantitative purposes, with the use of EM902 EFTEM images. It has been shown, that the application of this method to series of EM 902-images acquired around the iron edge, resulted in the segmentation of noise-free, Fe-net-intensity images. Whether these iron net-intensity images can be used for the calculation of quantitative iron-concentration-distribution images remains to be shown. Moreover, the results of the parametric processing, from a certain set of images, has to be compared to those of the non-parametric processing. (2). The other aspect is the use of computer models to investigate the influence of the various instrumental parameters involved in quantitative image analysis upon the final result. Aspects of accuracy and precision of spectral analysis have been discussed by various authors [13-15, 35]. Computer models permit one to simulate experiments, which physically are cumbersome to be performed on the microscope. It makes the operator aware of the influence of instrumental parameters and other aspects of the applied method on the final result.

In conclusion, EFTEM has become a mature analytical method for biological materials. EELS analysis by electron spectroscopic imaging can contribute to the *in situ* analysis of heterogeneous objects frequently present in cells and tissues. New instrumental improvements introduced recently will certainly contribute considerably to further maturation.

References

1. Adamson-Sharpe KM, Ottensmeyer FP. (1981). Spatial resolution and detection sensitivity in micro-analysis by electron energy loss selected imaging. J Microsc **122**: 309-320.

2. Ahn CC, Rez P. (1985). Inner shell edge profiles in electron energy loss spectroscopy. Ultramicrosc **17**: 105-116.

3. Arsenault AL, Ottensmeyer FP. (1983). Quantitative spatial distributions of calcium, phosphorus and sulphur in calcifying epiphysis by high resolution spectroscopic imaging. Proc Nat Acad Sci USA **80**: 1322-1331.

4. Arsenault AL, Ottensmeyer FP. (1984). Visualization of early intramembranous ossification by electron microscopic and spectroscopic imaging. J Microsc **98**: 911-921.

5. Bevington PR. (1969). Data reduction and error analysis for the physical sciences. McGraw-Hill. pp. 246-254.

6. Bihr J, Rilk A, Benner G. (1988). Angle of acceptance and energy resolution in the imaging electron energy-loss spectrometer of the EM 902. Inst Phys (Bristol) Conf Ser No **93**, Vol 1. Goodhew PJ, Dickinson HG (eds.). Chapter 2, pp 159-160.

7. Blaineau S, Julliard AK, Amsellem J, Nicaise G. (1987). Quantitative X-ray microanalysis of calcium with the Camebax-TEM system in frozen, freeze-substituted and resin-embedded tissue sections. Histochem **87**: 545-555.

8. Burton KWC, Nickless G. (1987). Optimisation via Simplex. Part I. Background, definitions and a simple application. Chemom Intell Lab Syst **1**: 135-149.

9. Cleton MI, Mostert LJ, Sorber CWJ, de Jong AAW, de Jeu-Jaspars C, de Bruijn WC (1989). Effect of phlebotomy on the ferritin iron content in the rat liver determined morphometrically with the use of electron energy-loss spectroscopy. Cell Tis Res **256**: 601-618.

10. Cleton MI, Roelofs JM, Blok-Van Hoek CJG, de Bruijn WC. (1986) Integrated image and X-ray microanalysis of hepatic lysosomes in a patient with idiopathic hemosiderosis before and after treatment by phlebotomy. Scanning Electron Microsc **1986**;III: 999-1014.

11. Colliex C. Jeanguillaume C, Trebbia P. (1981). Quantitative Local Microanalysis with EELS. Academic Press, New York. pp: 251-271.

12. Colliex C. Jeanguillaume C, Mory C. (1984). Unconventional modes for STEM imaging of biological structures. J Ultrastr Res **88**: 177-206.

13. Colliex C. (1985). An illustrated review of various factors governing the high spatial resolution capabilities in EELS microanalysis. Ultramicrosc **18**: 131-150.

14. Colliex C, Manoubi T, Krivanek OL. (1986). EELS in the Electron Microscope: A review of present trends. J Electron Microsc **35**: 307-313.

15. Colliex C. (1991). The impact of EELS in materials science. Microsc Microanal Microstruct **2**: 403-411.

16. Crozier PA, Chapman JN, Craven AJ, Titmarch JM. (1987). On the determination of inner-shell cross-section ratios of NiO using EELS. J Microsc **148**: 279-284.

17. de Bruijn WC, Schellens JPM, van Buitenen JMH, van der Meulen J. (1979). X-ray microanalysis of colloidal gold labelled lysosomes in rat liver sinusoidal cells after incubation with acid phosphatase activity. Histochem **66**, 137-148.

18. de Bruijn WC. (1981). Ion exchange beads as standards for X- ray microanalysis of biological tissue. Beitr Elektronemikrosk Direktabb Oberfl **16**: 369-372.

19. de Bruijn WC. (1981). Ideal standards for quantitative X-ray microanalysis of biological specimens. Scanning Electron Microsc **1981**;II: 357-367.

20. de Bruijn WC. (1984). Standards for quantitative X-ray microanalysis of biological specimens. Les Editions de Physique (Toulouse, France). Colloque C2, suppl. 2; Tome 45. pp 469-472.

21. de Bruijn WC. (1985). Integration of X-ray microanalysis and morphometry of biological material. Scanning Electron Microsc **1985**;II: 697-712.

22. de Bruijn WC, Cleton-Soeteman MI. (1985). Application of chelex standard beads in integrated morphometrical and X-ray microanalysis. Scanning Electron Microsc **1985**;II: 715-729.

23. de Bruijn WC, Koerten HK, Cleton-Soeteman MI, Blok-van Hoek CJG. (1987). Image analysis and X-ray microanalysis in cytochemistry. Scanning Microsc **1**: 1651-1667.

24. de Bruijn WC, Van Miert MPC. (1988). Extraneous background-correction program for matrix bound multiple point X-ray microanalysis. Scanning Microsc **2**: 319-322.

25. de Bruijn WC, Sorber CWJ. (1990). The application of Bio-standards for EELS analysis of biological materials. Proc XIIth Intern Congr for Electron Microscopy. San Francisco Press. pp. 68-69.

26. de Bruijn WC, Ketelaars D, Gelsema ES, Sorber CWJ. (1991). Comparison of the Simplex method with several other methods for background-fitting for electron energy loss spectral quantification of biological materials. Microsc Microanal Microstruct **2**: 281-291.

27. de Bruijn WC, Ketelaars GAM, Jongkind JF Sorber CWJ. (1991). EELS thickness measurements of sectioned biological materials. In: Proc. 2nd European Workshop Microbeam Analysis Society workshop, Dubrovnik 1991. p. 40 (abstract). Copy available from W.C. de Bruijn.

28. Disko MM, Shuman H. (1986). High spatial resolution analysis using parallel detection EELS. Ultramicrosc **20**: 43-50.

29. Door R, Frösch D, Martin R. (1991). Estimation of thickness and quantification of iron standards with EELS. J Microsc **162**: 15-22.

30. Drechsler M, Cantow H-J. (1991). EELS data acquisition, processing and display for the Zeiss CEM-902 based on Lotus1-2-3^R: application examples from biological systems and inorganic metal compounds. J Microsc. **162**: 61-76.

31. Edelmann L. (1989a). The contracting muscle a challenge for freeze-substitution and low-temperature embedding. Scanning Microsc. Suppl. **3**: 241-252.

32. Edelmann L. (1989b). The physical state of potassium in frog skeletal muscle studied by ion-sensitive micrô-electrodes and by electron microscopy: interpretation of seemingly incompatible results. Scanning Microsc **3**: 1219-1230.

33. Edelmann L (1989c). Freeze-substitution and low-temperature embedding for analytical electron microscopy. In: Electron Probe Microanalysis. Applications in Biology and Medicine. Zierold K, Hagler HK (eds.). Springer Verlag, Berlin. pp 33-46.

34. Edelmann L. (1990). Freeze-substitution and preservation of diffusible ions. J. Microsc **161**: 217-228.

35. Egerton RF. (1986). Energy Loss-Spectroscopy in the Electron Microscope. Plenum Press, New York. Chapter 3, pp. 129-148.

36. Egerton RF, Crozier PA. (1987). A compact parallel-recording detector for EELS. J Microsc **148**: 157-166.

37. Egerton RF. (1991). Factors affecting the accuracy of elemental analysis by transmission EELS. Microsc Microanal Microstruct **2**: 203-213.

38. Gelsema ES, Beckers ALD, Sorber CWJ, de Bruijn WC. (1992). Correspondence analysis for quantification in electron energy-loss spectroscopy and imaging. Methods Inf Med **31**: 29-35.

39. Gelsema ES, Beckers ALD, Sorber CWJ, de Bruijn WC. (1992). Quantification procedures for electron energy-loss spectroscopy and imaging: the use of correspondence analysis for element determination. J Microsc: **166**: 287-296.

40. Goldstein JI. (1975). Introduction to SEM. In: Practical Scanning Electron microscopy. Goldstein JI, Yakowitz H (eds.). Plenum press, New York. pp. 31-43.

41. Harauz G, Ottensmeyer FP. (1984a). Direct three-dimensional reconstruction for macromolecular complexes from electron micrographs. Ultramicrosc **12**: 309-320.

42. Harauz G, Ottensmeyer FP. (1984b). Nucleosome reconstruction via phosphorus mapping. Science **226**: 936-940.

43. Herrmann K-H, Krahl D. (1982). The detection quantum efficiency of electronic image recording systems. J Microsc **127**: 17-28.

44. Hezel UB, Bauer R, Zellmann E, Miller WI. (1986). Resolution and contrast enhancement on biologi-

cal specimens by means of electron spectroscopic imaging (ESI). In: Proc. 44th annual meeting EMSA. San Francisco Press. pp. 68-69.

45. Hezel UB, Bauer R. (1985). The new TEM with integrated imaging electron-energy spectrometer. Zeiss Inform. MEM **4**: 15-24.

46. Hofer F. (1991). Determination of inner-shell cross-sections for EELS quantification. Microsc Microanal Microstruct **2**: 215-230.

47. Joy DC, Maher DM. (1980). Electron energy loss spectroscopy: detectable limits for elemental analysis. Ultramicrosc **5**: 333-342.

48. Krahl D, Herrmann K-H, Kunath W. (1978). Electron optical experiments with a magnetic imaging filter. In: Electron Microscopy 1978, 9th Int. Cong. Microsc. Soc. Canada, Toronto. **1**: 42-43.

49. Krivanek OL, Gubbens AJ, Dellby N. (1991). Developments in EELS instrumentation for spectroscopy and imaging. Microsc Microanal Microstruct **2**: 315-332.

50. Krivanek OL, Mory C, Tencé M, Colliex C. (1991). EELS quantification near the single-atom detection level. Microsc Microanal Microstruct **2**: 257-267.

51. Körtje, KH, Körtje D, Rahmann H. (1991). The application of energy-filtering electron microscopy for the cytochemical localization of Ca^{2+}-ATPase activity in synaptic terminals. J Microsc **162**: 105-114.

52. Kruit P, Shuman H. (1985). The influence of objective lens aberrations in energy-loss spectrometry. Ultramicrosc **17**: 263-268.

53. Lehmann H, Kunz U, Jacob A. (1991). A simplified preparation procedure of plant material for elemental analysis by ESI and EELS techniques. J Microsc **162**: 77-82.

54. Leapman RD, Fiori CE, Gorlen KE, Gibson CC, Swyt CR. (1984). Combined elemental and STEM imaging under computer control. Ultramicrosc **12**: 281-292.

55. Leapman RD, Fiori CE, Swyt RE. (1984). Mass-thickness determination by electron energy-loss for quantitative X-ray microanalysis in biology. J Microsc **133**: 239-253.

56. Leapman RD, Ornberg RL. (1988) Quantitative electron energy loss spectroscopy in biology. Ultramicrosc **24**: 251-268.

57. Leapman RD, Swyt CR. (1988) Separation of overlapping core edges in electron energy loss spectra by multiple-least-squares fitting. Ultramicrosc **26**: 393-404.

58. Leapman RD, Andrews SB. (1991). Biological electron energy-losses spectroscopy: the present and the future. Microsc Microanal Microstruct **2**: 387-394.

59. Leapman RD, Hunt JA. (1991). Comparison of detection limits for EELS and EDXS. Microsc Microanal Microstruct **2**: 231-244.

60. Liu DR, Brown LM (1987). Influence of some practical factors on background extrapolation in EELS quantification. J Microsc **147**, 37-49.

61. Malis T, Cheng SC, Egerton RF. (1988). EELS Log-ratio technique for specimen-thickness measurement in the TEM. J Electron Microsc Techn **8**: 193-200.

62. Morgan E, Burton K, Nickless G. (1990). Optimization using the modified Simplex method. Chemom Intell Lab Syst **7**: 209-222.

63. Mostert LG, Cleton MI, De Bruijn WC, Koster JF, Van Eijk HG. (1989). Studies on ferritin in rat liver and spleen during phlebotomy. Int J Biochem **21**: 39-47.

64. Nelder JA, Mead R. (1965). A Simplex method for function minimisation. Computer J **7**: 308-313.

65. Ottensmeyer FP. (1984). Electron spectroscopic imaging: parallel energy filtering and microanalysis in the fixed-beam electron microscope. J Ultrastr Res **88**: 121-134.

66. Peachy LD, Heath JP, Lamprecht G. (1988). The use of an energy-filtering electron microscope to reduce chromatic aberration in images of thick biological specimens In: Proc. 44th Annual meeting, EMSA. San Francisco Press. pp. 88-89.

67. Pejas W, Rose H. (1978). Outline of an imaging magnetic energy filter free of second-order aberrations. In: Electron Microscopy 1978. Microsc Soc Canada, Toronto. **1**: 44-45.

68. Probst W. (1986). Ultrastructural localization of calcium in CNS of vertebrates. Histochem **85**: 231-239.

69. Pun T, Ellis JR, Eden M. (1985). Weighted least squares estimation of background in EELS imaging. J Microsc **137**: 93-100.

70. Reichelt R, Engel A. (1984). Monte Carlo calculations of elastic and inelastic electron scattering in biological and plastic materials. Ultramicrosc **13**: 279-294.

71 Reichelt R, Carlemalm E, Villiger W, Engel A. (1985). Concentration determination of embedded biological matter by scanning transmission electron microscopy. Ultramicrosc **16**: 69-80.

72. Reimer L, Fromm I, Rennekamp R. (1988). Operation modes of electron spectroscopic imaging and electron energy-loss spectroscopy in a transmission electron microscope. Ultramicrosc **24**: 339-354.

73. Reimer L, Ross-Messemer M. (1990). Contrast in the electron spectroscopic imaging mode of a TEM I. Influence of zero-loss filtering on scattering contrast. J Microsc **155**: 169-182.

74. Reimer L. (1991). Energy-filtering transmission electron microscopy. Advances in Electronics and Electron Physics Vol 81. Academic Press. 43-125.

75. Roomans GM, Shelburne JD. (1980). Basic methods in biological X-ray microanalysis. Scanning Electron Microsc **1980**;II: 309-321.

76. Ross-Messemer M, Frey J, Probst W. (1991). Parallel EELS with an Energy-filtering transmission electron microscope (EFTEM). Proc. 25th Meeting DEG Darmstad, pp 114. Optik **88**: Supplement (abstract).

77. Shavers CL, Parsons ML, Deming SN. (1979). Simplex optimization of chemical systems. J. Chem. Ed. **56**: 307-309.

78. Shuman H, Somlyo AP. (1987). Electron energy loss analysis of near-trace-element concentrations of calcium. Ultramicrosc **21**: 23-32.

79. Sorber CWJ, de Jong AAW, den Breejen NJ, de Bruijn WC. (1990). Quantitative energy-filtered image analysis in cytochemistry I. Morphometric analysis of contrast related images. Ultramicrosc **32**: 55-68.

80. Sorber CWJ, van Dort JB, Ringeling PC, Cleton-Soeteman MI, de Bruijn WC. (1990). Quantitative energy-filtered image analysis in cytochemistry II. Morphometric analysis of element-distribution images. Ultramicrosc **32**: 69-79.

81. Sorber CWJ, Ketelaars GAM, Gelsema ES, Jongkind JF, de Bruijn WC. (1991). Quantitative analysis of electron energy-loss spectra from ultrathin-sectioned biological material. I. Optimization of the background-fit with the use of Bio-standards. J Microsc **162**: 23-42.

82. Sorber CWJ, Ketelaars GAM, Gelsema ES, Jongkind JF, de Bruijn WC. (1991). Quantitative analysis of electron energy-loss spectra from ultrathin-sectioned biological material. II. The application of Bio-standards for quantitative analysis. J Microsc **162**: 43-54.

83. Sorber CWJ, Ketelaars GAM, Gelsema ES, Jongkind JF, de Bruijn WC. (1991). Quantitative EELS analysis of images of biological materials. In: Proc. 2nd European Workshop Microbeam Analysis Society workshop, Dubrovnik 1991. pp. 209-210. Copy available from W.C. de Bruijn.

84. Spendley W, Hext GR, Himsworth FR. (1962). Sequential application of Simplex designs in optimisation and evolutionary operations. Technometrics **4**: 441-461

85. Steele JD, Titchmarsh JM, Chapman JN, Paterson JH. (1985). A single-stage process for quantifying electron energy loss spectra. Ultramicrosc **17**: 273-276.

86. Stobbs WM, Boothroyd CB. (1991). Approaches for energy loss and energy filtered imaging in TEM in relation to the materials problem to be solved. Microsc Microanal Microstruct **2**: 333-350.

87. Titchmarsh JM, Malis TF. (1989). On the effect of objective lens chromatic aberration on quantitative electron-energy-loss spectroscopy (EELS). Ultramicrosc **28**: 277-282.

88. Trebbia P. (1988). Unbiased method for signal estimation in electron energy loss spectroscopy, concentration measurements and detection limits in quantitative microanalysis: methods and programs. Ultramicrosc **24**: 399-408.

89. Trebbia P, Bonnet N. (1990). EELS elemental mapping with unconventional methods. I Theoretical bases: image analysis with multivariate statistics and entropy concepts. Ultramicrosc **34**: 165-178.

90. Trebbia P, Mory C. (1990). EELS elemental mapping with unconventional methods II. Applications to biological specimens. Ultramicrosc **34**: 179-203.

91. Trinick J, Berriman J. (1987). Zero-loss electron microscopy with the Zeiss EM902. Ultramicrosc **21**: 393-398.

92. Unser M, Ellis JR, Pun T, Eden M. (1986). Optimal background estimation in EELS. J Microsc **145**: 245-256.

93. Verbeek PW, Vrooman HA, van Vliet LJ. (1988). Low-level image processing by Max-Min filters. Signal Process **15**: 249-258.

94. Verbucken AH, van Grieken E, Poulas GJ, de Bruijn WC. (1984). Embedded ion exchange beads as standards for laser microprobe mass analysis of biological specimens. Anal Chem **56**: 1362-1370.

95. Verrijk R, Huiskamp R, Smolders IJH, Begg AC, Sorber CWJ, de Bruijn WC. (1992). Cellular uptake and retention of BSH and microlocalization with EELS/ESI. In: Cellular Pharmokinetics of BNCT Compounds: Boron Neutron Capture Therapy Towards Clinical Trials of Glycoma Treatments. Gabel D, Moss R (eds.). Plenum Press, New York. pp. 189-195.

96. von Ziglinicki T. (1988). Monovalent ions are spatially bound within the sarcomere. Gen Physiol Biophys **7**: 495-503.

97. Wilson AR. (1991). Detection and quantification of low energy, low level electron energy loss edges. Microsc Microanal Microstruct **2**: 269-279.

98. Wróblewski R, Wróblewski J. (1984). Freeze-drying and freeze-substitution combined with low-temperature embedding. Histochem **81**: 469-475.

99. Yarbo LA, Deming SN. (1974). Selection and preprocessing of factors for simplex optimization. Anal Chim Acta **73**: 391-398.

100. Young IT (1988). Quantitative image analysis. Anal Quant Cytol Histol **10**: 269-279.

101. Zaluzec NJ. (1985). Digital filters for application to data analysis in electron energy-loss spectrometry. Ultramicrosc **18**: 185-190.

102. Zierold K, Steinbrecht RA. (1987). Cryofixation of diffusible elements in cells and tissues for electron probe microanalysis. In: Cryotechniques in Biological Electron Microscopy. Steinbrecht RA, Zierold K (eds.). Springer Verlag, Berlin. pp. 272-282.

103. Zierold K, Schäfer D. (1988). Preparation of cultured and isolated cells for X-ray microanalysis. Scanning Microsc. **2**: 1775-1790.

104. Zierold K. (1988). X-ray microanalysis of freeze-dried and frozen-hydrated cryosections. J Electron Microsc Techn **9**: 65-82.

105. Zierold K, Tardent P, Burakov SV. (1991). Elemental mapping of cryosections from cnidarian nematocytes. Scanning Microsc **5**: 439-444.

106. Zierold K, Tobler M, Müller M. (1991). X-ray microanalysis of high-pressure frozen and impact-frozen erythrocytes. J Microsc **161**: 12-20.

107. Zierold K. (1991). Cryofixation methods for ion localization in cells by electron probe microanalysis: A review. J Microsc **161**: 357-366.

Discussion with Reviewers

G.M. Roomans: You take the average of five sequentially measured spectra; is any mass loss noticeable and do you need to correct for this?

Authors: In spite of the use of a remote control system, mass-loss is present and measurable in series of (200 eV wide) serially acquired spectra. Previously, the degree of mass loss in multiple acquisitions from the same analyzed area has been estimated with the use of Ca-Bio-standards [81]. In short, there is an initial rise in R_{Ca} value followed by a decrease after the fourth and fifth analysis. From these results, we concluded that the number of acquisitions has to be kept as small as possible, but up to five spectra as a maximum might be acceptable ($W_\Gamma = 25$ eV, $W_\Delta = 50$ eV, diameter of objective-lens diaphragm $= 90\ \mu$m).

R.D. Leapman: To what extent is the spatial resolution of parallel EELS limited by chromatic aberration effects in ESI.

Authors: The dependence of the chromatic aberration effects in relation to the slit width are discussed in the literature [35]. In short, for this type of spectrometer, the final image is considered to be achromatic and independent (to the first order) of the width of the energy-selecting slit. To acquire a line spectrum, the system is slightly misaligned. However, this does not interfere with the spatial resolution and even might improve the energy resolution. The energy resolution is dependent upon the stability of the high-voltage supply to the electrostatic mirror. Due to the slight curvature created in the electrostatic mirror, the peripheral parts of the image might deviate slightly from the central part. In the cytoplasm in Figure 12, ferritin particles outside the siderosome are not clearly resolved. This might be due to the (too low) number of pixels per particle and/or the mathematical exercises applied to the images (addition, division, etc.) or due to drift.

R.D. Leapman: What are the minimum detectable atomic fractions of the biologically important elements, P, Ca and Fe in the: (a) ESI-mode, and (b) in the parallel EELS mode for the energy-filtering microscope?

Authors: The answers to these rather important questions have not yet been obtained by us. This is partially due to the fact that a reliable value for the total mass was difficult to achieve. Anticipating upon the results for the mentioned elements we think: 1. For phosphorus, quantification will be difficult, if not impossible, due to the low edges in the spectra. 2. Quantification of Ca, is hampered by the presence of carbon plasmon losses in the Γ region, but will be obtainable. 3. Quantification for Fe is feasible. When it is assumed, that the ^{P}EEL-spectrum of the Bio-standard shown (Fig. 6b) is "representative for the mean of 1800 Fe atoms", and the standard deviation in the Γ-range is estimated by eye, the minimum number of iron atoms to be detected in that analyzed area can grossly be estimated not to come below the 180 atoms. Noise reduction or elimination, in ^{P}EEL spectra and images will be the best approach for improvement. The same holds for the images shown in Figure 12, where the ferritin iron concentration (in white) is in the range of the Bio-standard. In principle, there might be (to the best of our knowledge) no difference in the final results whether spectra are acquired serially or in parallel, apart from the gain in acquisition time. For images, there is no theoretical difference since to each pixel of the set of images, the same mathematical procedure is applied as is applied to the values in the channels of the spectra. However, an additional factor which might deteriorate the final result is, e.g., the objective segmentation, when, at low concentrations, in the grey-value frequency histogram, the two populations are hard to separate (see Fig. 9d).

R.D. Leapman: What is the estimated experimentally determined detective quantum efficiency (DQE) of the SIT camera for the parallel-recorded spectra in Figure 7?

Authors: We have not experimentally determined the DQE of our SIT camera. Such camera systems have been reported to possess an improved DQE, by a factor of 7-8, as compared to the DQE of the PMT-recording system ($= 0.1$).